npj | climate and atmospheric science

www.nature.com/npjclimatsci

ARTICLE OPEN

Check for updates

Interannual impact of tropical southern Atlantic SST on surface air temperature over East Asia during boreal spring

Chen Sheng[1], Shaoyu Zhang[1,2], Yimin Liu[1,2]✉, Guoxiong Wu[1,2] and Bian He[1,2]

Using reanalysis data and simulations, this study revealed a pronounced negative interannual relationship between tropical southern Atlantic (TSA) sea surface temperature (SST) and East Asian surface air temperature (SAT) during boreal spring (March–May). Results confirm that the March–May TSA–SST anomaly can be considered an independent tropical driver unrelated to El Niño–Southern Oscillation. A possible mechanism linking TSA–SST and East Asian spring SAT involves an atmospheric wave train, energy conversion, and potential vorticity (PV)–θ dynamics. The anomalous TSA–SST induces an anomalous Walker circulation, which initiates a wave train that extracts energy from a westerly jet and propagates toward East Asia. Subject to PV–θ dynamics, the East Asian PV anomaly embedded within this wave train leads to bowed isentropes and resultant notable anomalous East Asian SAT. In particular, the bootstrapping results suggest that TSA–SST anomaly can cause an approximately sevenfold increase in the occurrence probability of extreme East Asian spring SAT.

npj Climate and Atmospheric Science (2023)6:186 ; https://doi.org/10.1038/s41612-023-00515-y

INTRODUCTION

East Asia, with its dense population that accounts for approximately one-fifth of the global population, is heavily reliant on spring conditions for sowing and cultivating crops. Spring surface air temperature (SAT) plays a vital role in East Asian agricultural production, with profound impacts on society, the economy, and people's livelihoods[1]. Therefore, understanding the factors that drive the variation in SAT in spring over East Asia is crucially important.

Previous studies indicated that various atmospheric interior signals, such as the Arctic Oscillation[2–9], North Atlantic Oscillation[10–14], and Siberian High[3,4,15,16], play roles in East Asian SAT variation. For example, the Arctic Oscillation can influence East Asia via thermal advection and surface radiation during boreal spring[7], and cold wave outbreaks associated with the Siberian High during boreal winter[3,14,15]. The North Atlantic Oscillation can influence East Asia during boreal winter and summer via a quasi-stationary Rossby wave[11,13] along the westerly jet that is modulated by the meridional gradient of potential vorticity (PV)[11]. In addition, the impact of Arctic Sea ice on East Asian SAT in boreal winter has also been discussed[17–20]. However, the role of oceanic forcing in East Asian SAT variation, particularly during boreal spring, has received less attention.

Tropical oceans have an important influence on global climatic anomalies. In addition to the extensive research conducted on the climatic effects of the El Niño–Southern Oscillation (ENSO)[21–27], Indian Ocean sea surface temperature (SST)[28–30], and northern Atlantic SST[7,9,31–34], the climatic effects of tropical southern Atlantic (TSA) SST have also drawn research attention in the scientific community. Some studies implied that TSA–SST during boreal spring is statistically independent of tropical northern Atlantic SST[35–37] and is possibly independent of ENSO[38–41]. Earlier studies that investigated the climatic effects of TSA–SST found that TSA–SST can influence Indian monsoon rainfall independently of ENSO[39] and that the TSA–SST anomaly can lead to an East Asian Meiyu onset anomaly via the Walker circulation and the Gill response[40]. It has also been reported that TSA–SST can drive cross-equatorial atmospheric PV transport over the Indian Ocean sector and influence SAT over the mid–high latitudes of Eurasia through the PV circulation[41]. Moreover, the TSA–SST is a major driver of the dominant mode of East Asian monsoon rainfall through the excitation of an atmospheric wave train[42]. However, studies regarding the connection between the TSA–SST and East Asian spring SAT remain insufficient and deserve further investigation.

The objectives of this study were to identify the interannual impact of the TSA–SST on East Asian SAT during boreal spring, which specifically refers to March–May (MAM), and to elucidate the possible controlling mechanism through data analysis and numerical experiments. Based on the results of this study, we propose a convincing candidate driver of the East Asian spring climate anomaly that could help further improve our understanding of the variation in East Asian SAT during MAM.

RESULTS

Relationship between the TSA–SST and East Asian SAT during MAM

The first and second modes of the empirical orthogonal function (EOF) of tropical Atlantic SST during MAM are shown in Fig. 1a, b, respectively. Their explained variances are 37.1% and 25.1%, respectively. The major center of variation in EOF1 (Fig. 1a) featuring a uniform mode is in the tropical northern Atlantic, while the center of major variation in EOF2 (Fig. 1b) is in the TSA region. The distinct separation between EOF1 and EOF2 is statistically significant, as confirmed by the North test[43]. This finding indicates that the interannual variability in SST over the TSA is statistically independent of that in the tropical northern Atlantic[35,40].

Figure 1c presents the EOF1 mode of SST for the entire tropical ocean during MAM. The explained variance in this mode is 34.9%. A positive anomaly can be observed over the equatorial central–eastern Pacific, while negative anomalies extend along its flanks in a K-shaped pattern. This pattern over the Pacific,

[1]State Key Laboratory of Numerical Modeling for Atmospheric Sciences and Geophysical Fluid Dynamics (LASG), Institute of Atmospheric Physics, Chinese Academy of Sciences, Beijing 100029, China. [2]College of Earth and Planetary Sciences, University of Chinese Academy of Sciences, Beijing 100049, China. ✉email: lym@lasg.iap.ac.cn

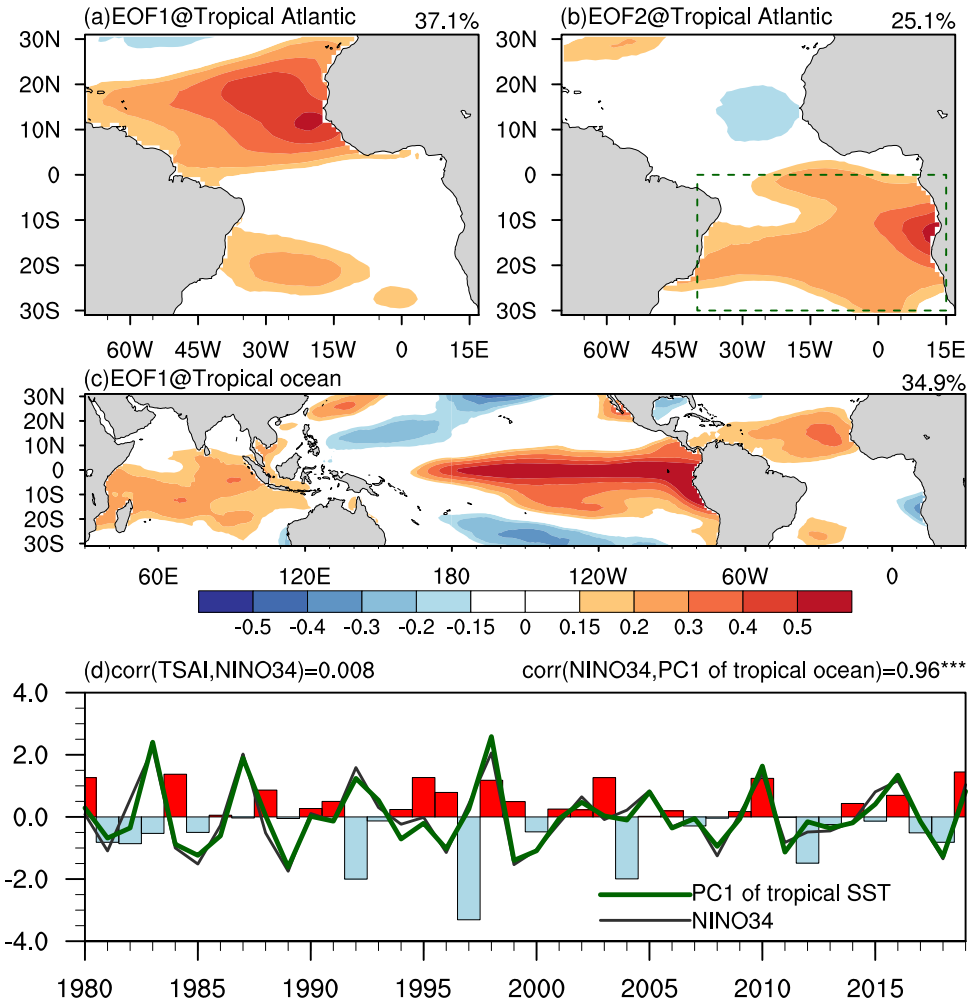

Fig. 1 EOF modes of SST in the tropical Atlantic and entire tropical ocean during MAM. a EOF1 mode of tropical Atlantic SST during MAM. **b** Same as **a** but for EOF2. **c** same as **a** but for SST over the entire tropical ocean. **d** Time series of the TSAI (bars), MAM NINO34 (black line), and PC1 (green line) corresponding to (**c**). "***" indicates a significance level exceeding 0.01.

accompanied by uniform positive anomalies over the Indian Ocean, closely resembles the typical ENSO signal[44]. We calculated the correlation coefficient between the first principal component (PC1) corresponding to Fig. 1c and the MAM Niño3.4 index (NINO34). The result yielded a remarkably high correlation coefficient of 0.96 (Fig. 1d). An important feature of note in Fig. 1c is that the Atlantic sector exhibits a pattern that closely resembles the EOF1 mode of tropical Atlantic SST (Fig. 1a). This finding suggests that interannual variability in SST over the tropical northern Atlantic is coupled with ENSO[32,38].

Owing to the statistical independence of the variability in SST over the tropical northern Atlantic and the TSA (Fig. 1a, b), the correlation coefficient between the MAM NINO34 and the TSA index (TSAI), which is measured by the normalized averaged MAM SST over 0°–30°S and 40°W–15°E (as indicated by the box shown in Fig. 1b), is expectedly small, measuring only 0.008 (Fig. 1d). We also calculated the correlation coefficient between the TSAI and the preceding December–February NINO34, and the result was found to be statistically insignificant at 0.23. The above results indicate that TSA–SST variability is statistically independent of ENSO, which is a finding that has been partly alluded to in previous work[39,41]. Consequently, TSA–SST can be considered an independent tropical driver during MAM.

Figure 2 shows the regression of the 2-m air temperature on the TSAI during MAM. It is evident that the anomalous TSA–SST is associated with the widespread SAT anomaly over Eurasia. At mid–low latitudes, a belt of positive values extends from western Africa to southern Asia. There is also a positive regression relationship over the Tibetan Plateau, but the associated regression coefficients are statistically insignificant. The positive regression relationship may be related to the eastward propagation of a downwelling Kelvin wave induced by the tropical Atlantic SST anomaly[45]. The dynamic origin of the regression relationship at mid–high latitudes is distinct from that at mid–low latitudes. At mid–high latitudes, a wave-train-like SAT anomaly is evident across Eurasia, which is of particular interest in this study. Small centers are observed over Western Europe (marked by A) and the East European Plain (marked by B), whereas the most prominent center with a strong negative regression relationship is over East Asia, including Mongolia (marked by C), eastern China, North Korea, South Korea, and Japan. This significant negative pattern is concentrated in the region from Mongolia to eastern China, which is outlined by the dashed box in Fig. 2. For simplicity, in the following, the term East Asia refers to the region outlined by the dashed box unless stated otherwise. The correlation coefficient between the TSAI and the box-averaged SAT was −0.62, passing the Student's *t*-test at the 0.01 significance level. The negative regression pattern over East Asia resembles the shape of the Siberian High[3]. Owing to the blocking effect of the Tibetan Plateau, the cold (warm) SAT anomaly embedded within the Siberian High can spread to the Yangtze River valley in eastern China. The composite patterns of SAT differences (Fig. S1)

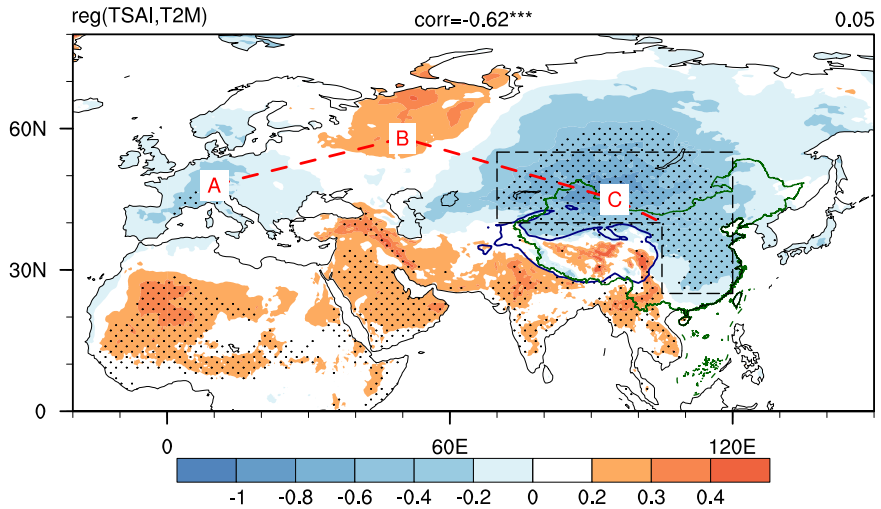

Fig. 2 Regression of SAT on the TSAI during MAM. T2M indicates the 2-m air temperature (unit: °C). Areas with values exceeding the 0.05 significance level are highlighted by black dots. Letters A, B, and C mark the centers of a wave-train-like SAT anomaly. The dashed box outlines the significant center of the East Asian SAT anomaly. The blue line denotes the boundary of the Tibetan Plateau topography with an elevation of 3000 m. "***" indicates a significance level exceeding 0.01.

between the warm and cold TSA–SST anomalies based on the different threshold values of the TSAI are consistent with the regressed results (Fig. 2). These results suggest that warm (cold) TSA–SST anomalies favor statistically significant cold (warm) East Asian SAT anomalies.

Mechanism by which the TSA–SST influences East Asian SAT during MAM

Figure 3a presents the regressed 200-hPa geopotential height (contours) on the TSAI and the correlation between the 200-hPa horizontal wind (vectors) and the TSAI. In the warm TSA–SST phase (TSAI > 0), an anomalous easterly prevails from the equatorial Atlantic to the central Pacific. This anomalous easterly flow is mainly caused by the anomalous Walker circulation (Fig. S2). Figure S2 presents the correlation coefficients between the TSAI and the zonal-vertical circulation averaged over 10°S–10°N. Evidently, the warm TSA–SST leads to a significant ascending motion anomaly over the TSA region. The ascending motion anomaly turns to an anomalous easterly aloft, and the significant easterly anomaly can cover the equatorial Atlantic to the central–eastern Pacific. This process is in accordance with the model simulation conducted by Zhang et al.[40]. Consequently, due to the meridional shear of the easterly anomaly, a significant anomalous high and anticyclonic circulation is triggered to the south of North America (SNA) (Fig. 3a). A large-scale wave train extending from the SNA to Eurasia is evident in Fig. 3a. An analysis of the wave activity flux (Eq. 1) shown in Fig. 3b suggests that the wave energy originates from the SNA and disperses downstream toward the Mongolia-centered region. The anomalous PV (Eq. 2) (Fig. 3b) embedded within this wave train is well organized and arranged alternately downstream along the wave energy path. The cold TSA–SST phase (TSAI < 0) corresponds to the opposite situation of atmospheric circulation. The 200-hPa centers of this wave train in the Eurasia sector (Figs. 3a, b) are broadly collocated with the anomalous SAT (Fig. 2), indicating that the atmospheric wave train plays a critical role in connecting the TSA–SST anomaly and the East Asian SAT anomaly.

To further elucidate the detailed dynamics of the atmospheric wave train, Fig. 3c presents the spatial distribution of the energy diagnostic. Prominent conversion of the kinetic energy[46] (CK; Eq. 3) signal can be observed south of the subtropical westerly jet, specifically, near the SNA region (outlined by the red dashed box in Fig. 3c). The SNA-averaged CK is positive (subplot in Fig. 3c), indicating that the anomalous circulation over the SNA extracts energy from the climatic state of the subtropical westerly jet (contours). This finding further confirms that the SNA serves as a wave source in the atmospheric wave train. Further analysis reveals that the positive SNA-averaged CK is primarily contributed by the CKy (Eq. 3) that results from positive $-u'v'\partial\overline{u}/\partial y$ (Fig. 3c). This finding aligns with previous theoretical work by Simmons et al.[47], suggesting that the northward-propagating wave train ($-u'v' > 0$[48]) could extract energy from the region to the south of the subtropical westerly jet ($\partial\overline{u}/\partial y > 0$), and therefore, the subtropical westerly jet could anchor the location of the associated wave train.

Figure 3d presents the composite differences in 200-hPa geopotential height (contours) and wind (vectors) between the POS and NEG experiments (see details in the Experimental design in the Methods section). The tropical easterly anomaly associated with the Walker circulation anomaly, whose meridional shear is critical for triggering the wave train, is simulated in Fig. 3d. In comparison with the reanalysis (Fig. 3a), the major difference is that the wave train over the North America sector shifts eastward. Because of the anchoring effect of the subtropical westerly jet, this difference can be ascribed to the systemic wind bias introduced by the eastward shift of the maximum center of the subtropical westerly jet over North America in the model (Fig. 3d). Despite this difference, the atmospheric wave train is generally well simulated, especially the anomalous cyclonic circulation over the Mongolia-centered region. Therefore, the model experiment supports the assertion that the TSA–SST anomaly can stimulate the atmospheric wave train that influences East Asian SAT during MAM.

In examining how the atmospheric circulation anomaly with embedded anomalous PV influences East Asian SAT, Fig. 4a presents the cross-section (along the line A–B–C in Fig. 2) of the correlation coefficients between the TSAI and both PV (shading) and potential temperature (contours). Figure 4a suggests that the 200-hPa PV anomaly (Fig. 3b) can extend to the surface and form three equivalent barotropic PV columns. Recalling the PV–θ mechanism[49,50], the atmospheric positive (negative) PV anomaly (Fig. 4b, c) would vertically suck (drain) the isentropes, resulting in upward (downward) bowing of the isentropes beneath the PV anomaly itself. Because upward-bowing (downward-bowing) isentropes indicate a cold (warm) air temperature anomaly, these PV columns would lead to SAT anomalies. Subject to the PV–θ mechanism, in the warm TSA–SST phase, the positive PV column

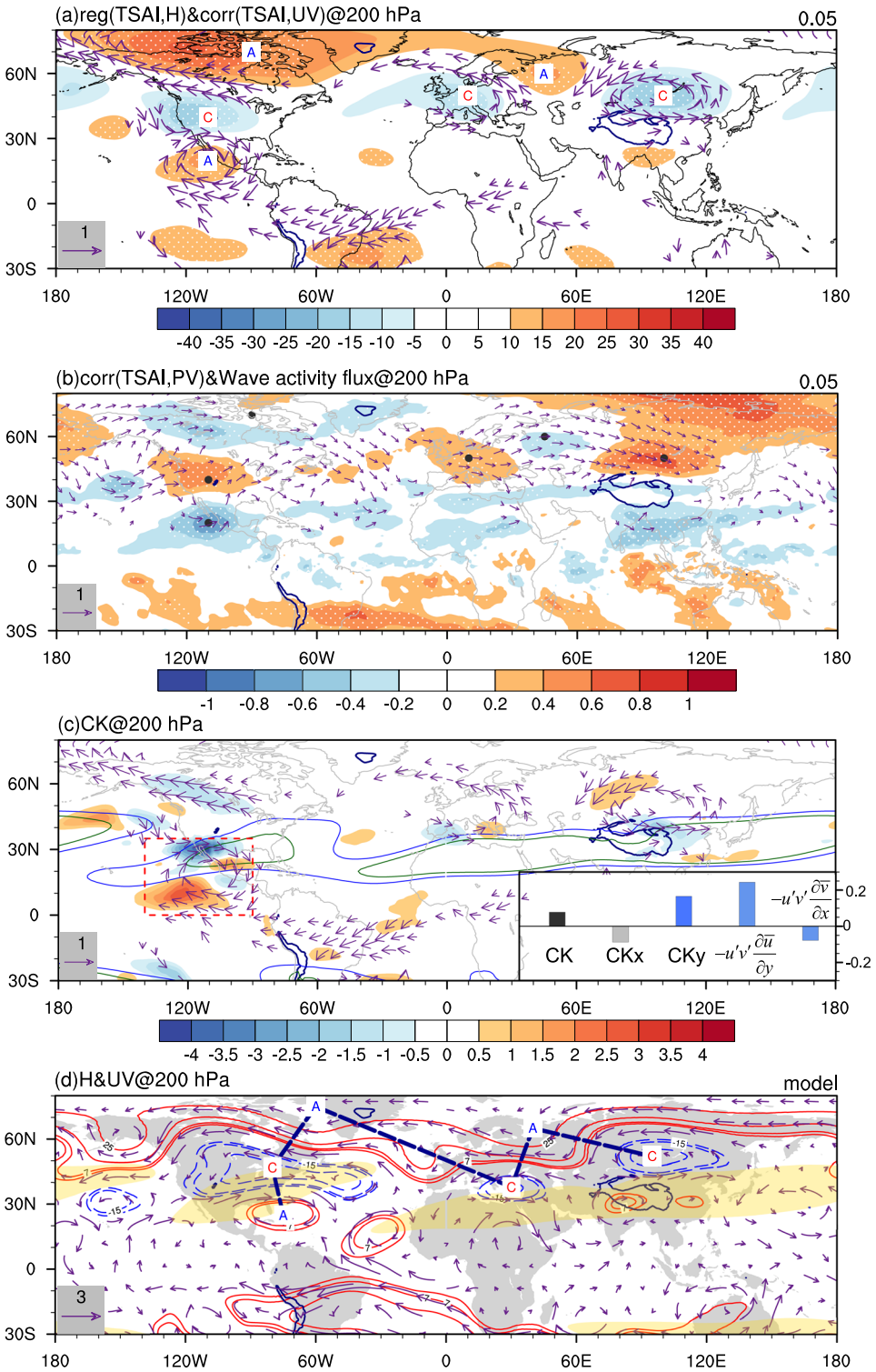

Fig. 3 Mechanism by which the TSA–SST influences atmospheric circulation during MAM. a Regression of 200-hPa geopotential height (shading; unit: gpm) on the TSAI during MAM. Correlation coefficients between the TSAI and the 200-hPa horizontal wind (vectors) during MAM. Vectors exceeding the 0.05 significance level are shown. **b** Correlation of 200-hPa PV (shading) and regressed wave activity flux (vectors) on the TSAI during MAM. **c** Regression of CK and its components on the TSAI during MAM. Vectors are the same as those in (**a**). Based on Eq. (3), the subplot shows the energy diagnostics result averaged over the red dashed box. The blue and green lines indicate zonal winds exceeding 25 and 30 m/s, respectively. **d** Differences in 200-hPa geopotential height (contours) and horizontal wind (vectors) between the POS and NEG ensemble means during MAM. The dashed blue line indicates the Rossby wave train. Yellow shading indicates the zonal wind exceeding 25 m/s in the climate model. Areas exceeding the 0.05 significance level are highlighted by dots in (**a**) and (**b**). The thick blue line in East Asia denotes the boundary of the Tibetan Plateau topography with an elevation of 3000 m.

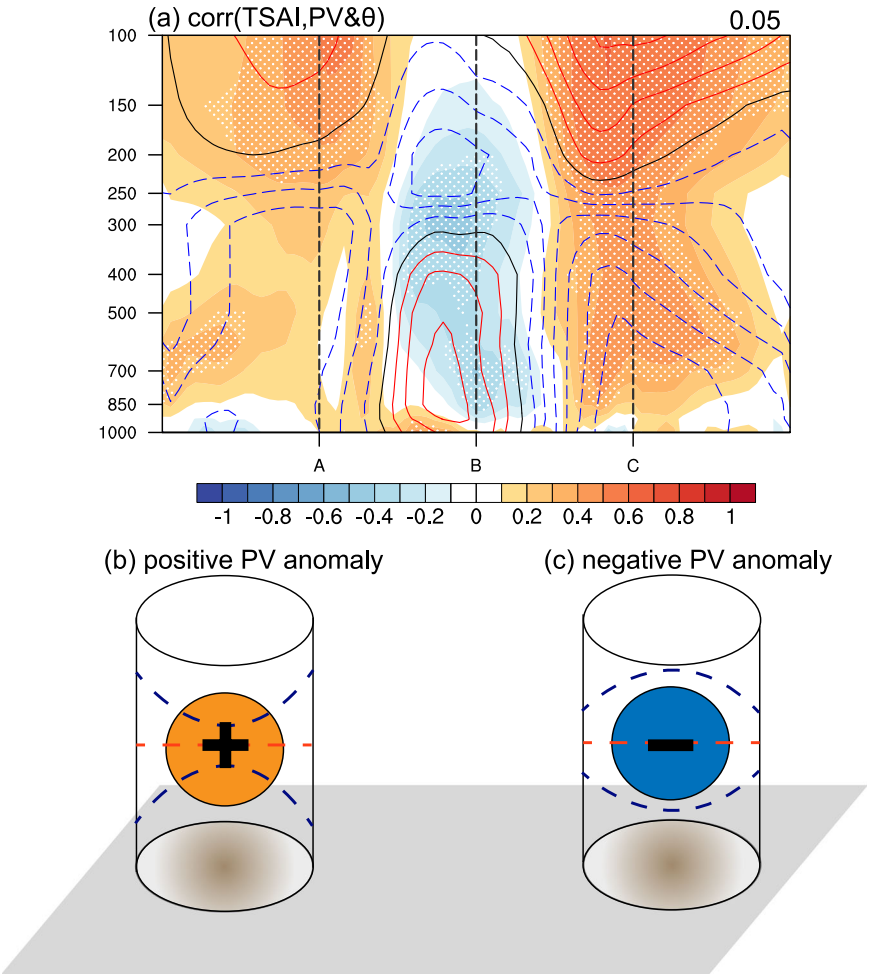

Fig. 4 Structure of anomalous PV and potential temperature. a Cross-section of the correlation coefficients between the TSAI and potential temperature (contours) and PV (shading) along lines A–B–C in Fig. 2 during MAM. Solid (dashed) lines indicate positive (negative) values. Areas with values exceeding the 0.05 significance level are highlighted by white dots. **b** and **c** Schematic showing the PV–θ mechanism for the case of a positive and negative PV anomaly, respectively. Colored circles in (**b**) and (**c**) indicate positive and negative PV anomalies, respectively. Dashed lines in **b** and **c** indicate isentropes.

(Fig. 4a; shading) over the Mongolia-centered region (marked by C) would therefore induce a major cold air temperature anomaly at the lower level (dashed contours), and the converse situation would occur in the cold TSA–SST phase. Finally, assisted by the blocking effect of the Tibetan Plateau (Fig. 2), the SAT anomaly embedded within the Siberian High[3] could spread to eastern China, ultimately covering the broader area of East Asia.

Impact of TSA–SST on extreme SAT over East Asia during MAM

Based on reanalysis data, Fig. 5 presents probability density functions of MAM SAT averaged over East Asia (within the dashed box shown in Fig. 2) estimated from Monte Carlo bootstrap samples[51,52] in terms of the climatic mean (black curve), warm TSA–SST phase (blue curve in Fig. 5a), and cold TSA–SST phase (red curve in Fig. 5b). The resampling process was executed 100,000 times. The extreme cold and hot threshold values, determined by the 10th percentile (Fig. 5a) and 90th percentile (Fig. 5b) of the climatic distribution of the probability density function, respectively, are indicated by the vertical black lines. An extreme cold (hot) spring is identified when the SAT is smaller (greater) than the extreme cold (hot) threshold value. In the warm TSA–SST phase (Fig. 5a), the probability density function is shifted markedly to the left, leading to a probability of an extremely cold spring of up to 79%. In the cold TSA–SST phase (Fig. 5b), the probability density function is shifted markedly to the right, leading to a probability of an extremely hot spring of up to 86%. These results indicate that the TSA–SST anomaly can cause a substantial increase (approximately a 7-fold increase from 10% to approximately 80%) in the occurrence probability of extreme MAM SAT in East Asia.

DISCUSSION

This study investigated the impact of the TSA–SST on East Asian SAT during MAM on the interannual timescale. Our findings support the assertion that the TSA–SST variability is statistically unrelated to ENSO and tropical northern Atlantic SST during MAM, and the TSA–SST can be considered an independent tropical driver. Further results suggest a significant negative relationship between the TSA–SST and East Asian SAT in that a warm (cold) TSA–SST anomaly favors a cold (warm) East Asian SAT anomaly. The underlying mechanism driving this relationship involves a wave train extending from North America to East Asia, energy conversion, and the PV–θ mechanism, as summarized by the schematic presented in Fig. 6. A warm TSA–SST anomaly (Fig. 6b) leads to an anomalous upper-level easterly (Fig. 6a), which prevails over the tropical Atlantic to the tropical eastern Pacific owing to an anomalous Walker circulation. The meridional shear of the

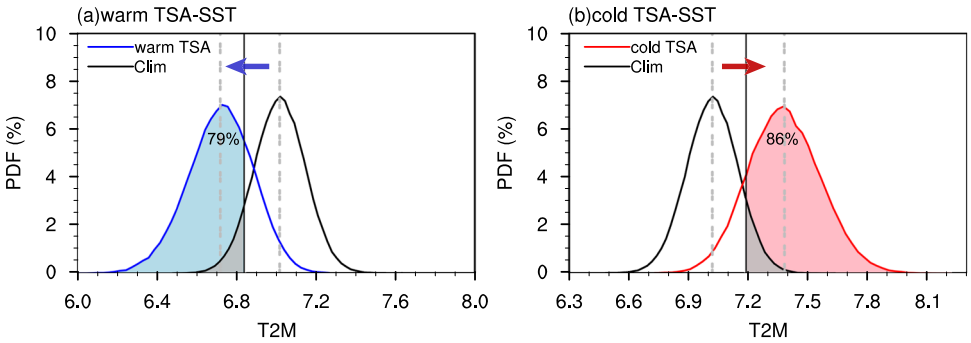

Fig. 5 Probability density functions of East Asian MAM SAT during different phases of TSA–SST. Probability density function was estimated from 100,000 bootstrap samples of East Asian MAM SAT in terms of the climatic mean (black curve), **a** the positive TSA–SST phase, and **b** the negative TSA–SST phase. The gray dashed line indicates the mean value. Black solid lines in **a** and **b** indicate the extreme cold and hot thresholds, respectively. T2M indicates the 2-m air temperature. Unit of the horizontal axis: °C.

anomalous easterly (Fig. 6a) triggers an anticyclonic circulation anomaly over the SNA region, and the resultant SNA anticyclonic circulation anomaly initiates a large-scale wave train by extracting energy from the basic subtropical westerly jet (green line in Fig. 6a). This wave train eventually reaches East Asia and leads to an anomalous cyclonic circulation and a positive PV anomaly over the Mongolia-centered region (Fig. 6a). Subject to the PV–θ mechanism, the isentropes in the lower part of the positive anomalous PV column (brown cone-like structure in Fig. 6) bow upward and induce the East Asian cold SAT anomaly (Fig. 6b). The blocking effect of the Tibetan Plateau facilitates the advection of the cold SAT anomaly toward eastern China and ultimately across much of East Asia. Conversely, a cold TSA–SST anomaly corresponds to the opposite set of atmospheric conditions and SAT anomalies.

Our findings also highlight the impact of the TSA–SST on the probability distribution of East Asian SAT (Fig. 5). Specifically, it was found that the TSA–SST anomaly can markedly shift the probability density functions of East Asian SAT (Fig. 5), leading to a substantial increase in the occurrence probability of extreme SAT over East Asia during MAM. Monte Carlo bootstrapping indicates that the warm (cold) TSA–SST phase can increase the occurrence probability of an extreme cold (hot) spring in East Asia from 10% to up to 79% (86%).

We also examined the relationship between ENSO and East Asian MAM SAT. Figure S3a presents the EOF1 of East Asian SAT during MAM. The correlation coefficient between the East Asian SAT PC1 and MAM NINO34 was found to be very low, i.e., 0.005 (Fig. S3b). However, as expected, the correlation coefficient between the East Asian SAT PC1 and TSAI was significantly high at 0.55, passing the Student's *t*-test at the 0.01 significance level (Fig. S3b). This result suggests that East Asian MAM SAT is statistically unrelated to ENSO but is closely determined by TSA–SST, reconfirming the important role of TSA–SST in the interannual variability of the spring climate of East Asia. Identification of a precursor of MAM TSA–SST to improve the skill in predicting East Asian spring SAT, which is subject to the predictability barrier of ENSO[53–55], is an interesting topic that will be studied in the future.

METHODS

Reanalysis data

Monthly ERA5[56] (the fifth generation ECMWF atmospheric reanalysis of the global climate) data were employed in this study. Pressure level data included zonal wind, meridional wind, geopotential height, and air temperature data. Single-level data included 2-m air temperature and surface pressure. SST data were obtained from the COBE (Centennial in situ Observation-Based Estimates) dataset[57]. The Niño3.4 index was obtained from https://psl.noaa.gov/data/climateindices/list/.

The horizontal resolution of the ERA5 and COBE SST data is 1° × 1°. The period considered in this study was 1980–2019. Boreal spring refers to the period from March to May (i.e., MAM).

To focus on the interannual variability during MAM, the linear trend and the interdecadal variation over more than 9 years were filtered out in the raw data. "***" indicates a significance level exceeding 0.01, as determined by the Student's *t*-test unless otherwise specified.

Monte Carlo bootstrapping

The bootstrapping, developed by Efron[51], is a Monte Carlo method that involves resampling—that is, taking repeated samples (with replacement) from the original sample dataset. It is particularly useful when dealing with small sample sizes.

In this study, using random sampling with replacement, bootstrapping takes a sample of East Asian averaged SAT during MAM with a sample size of N years and forms a new sample called bootstrap sample. Then, the time mean of the bootstrap sample is computed to obtain the bootstrap mean. The above process was repeated 100,000 times. Finally, a probability density function containing 100,000 bootstrap mean values is formed. In the climate mean state, the sample size N is equal to 40, which is the number of years of the investigated period. In the warm or cold TSA–SST phase, sample size N is the number of years of the corresponding phases. The Monte Carlo bootstrapping procedure used in this study is available at the website of NCAR (National Center for Atmospheric Research) Command Language: https://www.ncl.ucar.edu/Document/Functions/Bootstrap/bootstrap_stat.shtml. More details regarding this method can be found in Efron[51] and Diaconis and Efron[52].

Wave activity flux, PV, and CK

The horizontal wave activity flux[58], which is used to track the pathway of propagation of Rossby wave energy, was calculated as follows:

$$\textit{Wave activity flux} = \frac{p}{2|U|}\left\{\begin{array}{l}\overline{u}(\psi_x'^2 - \psi'\psi_{xx}') + \overline{v}(\psi_x'\psi_y' - \psi'\psi_{xy}') \\ \overline{u}(\psi_x'\psi_y' - \psi'\psi_{xy}') + \overline{v}(\psi_y'^2 - \psi'\psi_{yy}')\end{array}\right\} \quad (1)$$

in which p, $|U|$, and ψ are the pressure, horizontal wind speed, and geostrophic stream function, respectively. The subscript represents the partial derivative. The overbar and prime represent the temporal mean and the temporal anomaly, respectively.

The PV at a pressure level was calculated as follows[49,59]:

$$PV = a\vec{\zeta_a}\cdot\nabla\theta = g\left[\frac{\partial v}{\partial p}\left(\frac{\partial\theta}{\partial x}\right)_p - \frac{\partial u}{\partial p}\left(\frac{\partial\theta}{\partial y}\right)_p\right] - g\left[f + \left(\frac{\partial v}{\partial x}\right)_p - \left(\frac{\partial u}{\partial y}\right)_p\right]\frac{\partial\theta}{\partial p} \quad (2)$$

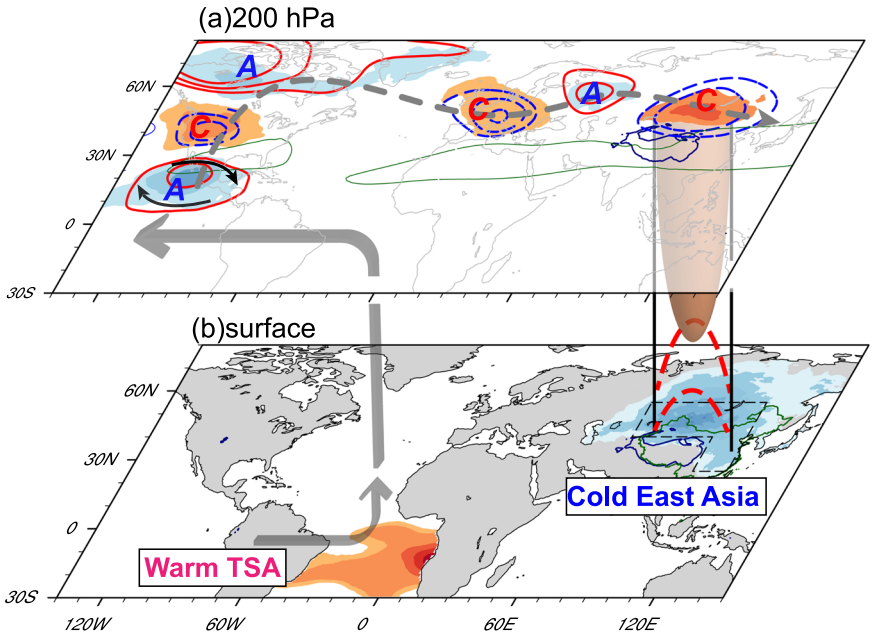

Fig. 6 Schematic showing how the TSA–SST influences East Asian SAT during MAM. a Anomalous 200-hPa PV (shading) and geopotential height (contours). The green line represents the zonal wind speed of 30 m/s. The gray dashed line indicates Rossby wave propagation. **b** TSA–SST anomaly and East Asian SAT anomaly. The zonal-vertical gray vector indicates the anomalous Walker circulation. The brown cone-like structure indicates a positive anomalous PV column. Red dashed lines indicate isentropes. The blue line denotes the boundary of the Tibetan Plateau topography with an elevation of 3000 m.

where $\alpha = \frac{1}{\rho}$ is the specific volume, $\vec{\zeta_a}$ is the three-dimensional absolute vorticity, θ is the potential temperature, g is gravitational acceleration, (u, v) is the horizontal wind, and f is the Coriolis parameter.

Energetic analysis was performed to explore the atmospheric wave dynamics. The CK (i.e., conversion of kinetic energy) from the climatic state to the atmospheric perturbation was calculated as follows[46]:

$$CK = \underbrace{\frac{v'^2 - u'^2}{2}\left(\frac{\partial \overline{u}}{\partial x} - \frac{\partial \overline{v}}{\partial y}\right)}_{CKx} \underbrace{-u'v'\left(\frac{\partial \overline{u}}{\partial y} + \frac{\partial \overline{v}}{\partial x}\right)}_{CKy} \quad (3)$$

The prime and overbar are the same as those in Eq. (1). A positive CK value indicates that the atmospheric perturbations extract energy from the climatic state; therefore, a positive CK favors the development of atmospheric perturbations. A negative CK value indicates the opposite situation.

Experimental design

The Flexible Global Ocean–Atmosphere–Land system (FGOALS-f2) is a climate model developed by the Institute of Atmospheric Physics/State Key Laboratory of Numerical Modeling for Atmospheric Sciences and Geophysical Fluid Dynamics, Chinese Academy of Sciences[60]. Its atmospheric component FAMIL2[61–63] was employed in this study. The horizontal resolution of FAMIL2 used in this study is approximately $1° \times 1°$. Vertically, FAIML2 has 32 levels with the model top at 2.16 hPa.

Based on FAMIL2, three experiments were designed to elucidate the climatic effect of TSA–SST. The control run experiment was driven by the prescribed climatological annual SST cycle, which was averaged over the period of 1980–2019. The control run was integrated for 30 years, and the final 20 years of the output were used in the analysis. Positive (negative) TSA–SST anomalies based on TSAI > 0.75 (TSAI < −0.75) were added to the control run SST and referred to as the POS (NEG) experiment. The POS and NEG experiments both had 20 members integrated from January to June, with the initial field taken from January of the final 20 years of the output of the control run experiment. For both the POS and NEG experiments, SST forcing was input from February to May. The mean value derived from the 20 members was analyzed.

DATA AVAILABLITY

ERA5 data are available from the Copernicus Climate Data Store, https://cds.climate.copernicus.eu/. The COBE SST data are available at https://psl.noaa.gov/data/gridded/data.cobe.html. The Niño3.4 index can be obtained from https://psl.noaa.gov/data/climateindices/list/.

CODE AVAILABLITY

All code used for the analyses in this study may be made available to qualified researchers upon reasonable request to the corresponding author.

Received: 29 June 2023; Accepted: 31 October 2023;
Published online: 11 November 2023

REFERENCES

1. Chen, S. & Wu, R. Interdecadal changes in the relationship between interannual variations of spring North Atlantic SST and Eurasian surface air temperature. *J. Clim.* **30**, 3771–3787 (2017).
2. Thompson, D. W. J. & Wallace, J. M. The Arctic oscillation signature in the wintertime geopotential height and temperature fields. *Geophys. Res. Lett.* **25**, 1297–1300 (1998).
3. Gong, D. Y., Wang, S. W. & Zhu, J. H. East Asian winter monsoon and Arctic Oscillation. *Geophys. Res. Lett.* **28**, 2073–2076 (2001).
4. Wu, B. Y. & Wang, J. Possible impacts of winter Arctic Oscillation on Siberian high, the East Asian winter monsoon and sea-ice extent. *Adv. Atmos. Sci.* **19**, 297–320 (2002).
5. Gong, D. Y. & Wang, S. W. Influence of Arctic Oscillation on winter climate over China. *J. Geogr. Sci.* **13**, 208–216 (2003).

6. Chen, S. F., Chen, W. & Wei, K. Recent trends in winter temperature extremes in eastern China and their relationship with the Arctic Oscillation and ENSO. *Adv. Atmos. Sci.* **30**, 1712–1724 (2013).
7. Chen, S., Wu, R. & Liu, Y. Dominant modes of interannual variability in Eurasian surface air temperature during boreal spring. *J. Clim.* **29**, 1109–1125 (2016).
8. Yin, S., Feng, J. & Li, J. Influences of the preceding winter northern Hemisphere annular mode on the spring extreme low temperature events in the north of eastern China. *Acta Meteor. Acta Meteor. Sin.* **71**, 96–108 (2013).
9. Fu, S. S., Zhu, Z. W. & Lu, R. Changes in the factors controlling Northeast Asian spring surface air temperature in the past 60 years. *Clim. Dyn.* **61**, 169–183 (2023).
10. Yuan, W. & Sun, J. Q. Enhancement of the summer North Atlantic Oscillation influence on northern hemisphere air temperature. *Adv. Atmos. Sci.* **26**, 1209–1214 (2009).
11. Song, J., Li, C. Y. & Zhou, W. High and low latitude types of the downstream influences of the North Atlantic Oscillation. *Clim. Dyn.* **42**, 1097–1111 (2014).
12. Shen, X. S. & Masahide, K. Studies of the interannual variability of springtime Eurasian surface air temperature. *Chin. J. Atmos. Sci.* **31**, 19–27 (2007).
13. Sun, J. Q., Wang, H. J. & Yuan, W. Decadal variations of the relationship between the summer North Atlantic Oscillation and middle East Asian air temperature. *J. Geophys. Res. Atmos.* **113**, 1–11 (2008).
14. Zhang, Y., Sperber, K. R. & Boyle, J. S. Climatology and interannual variation of the East Asian winter monsoon: results from the 1979-95 NCEP/NCAR reanalysis. *Mon. Weather Rev.* **125**, 2605–2619 (1997).
15. Jeong, J. H. & Ho, C. H. Changes in occurrence of cold surges over east Asia in association with Arctic Oscillation. *Geophys. Res. Lett.* **32**, 1–4 (2005).
16. Zhu, H. X., Chen, W., Feng, T. & Wang, L. Interannual variations of Siberian High during boreal winter and its influence on East Asian temperature. *Plateau Meteor.* **38**, 685–692 (2019).
17. Inoue, J., Hori, M. E. & Takaya, K. The role of Barents Sea Ice in the wintertime cyclone track and emergence of a warm-Arctic cold-Siberian anomaly. *J. Clim.* **25**, 2561–2568 (2012).
18. Wu, B. Y., Su, J. Z. & D'Arrigo, R. Patterns of Asian winter climate variability and links to Arctic Sea Ice. *J. Clim.* **28**, 6841–6858 (2015).
19. Liu, B. & Zhu, C. Weak linkage of winter surface air temperature over Northeast Asia with East Asian winter monsoon during 1993-2003. *Clim. Dyn.* **53**, 6107–6124 (2019).
20. Duan, A. M. et al. Sea ice loss of the Barents-Kara Sea enhances the winter warming over the Tibetan Plateau. *npj Clim. Atmos. Sci.* **5**, 1–6 (2022).
21. Thirumalai, K., DiNezio, P. N., Okumura, Y. & Deser, C. Extreme temperatures in Southeast Asia caused by El Nino and worsened by global warming. *Nat. Commun.* **8**, 1–8 (2017).
22. Zheng, J. et al. The relationship between Indo-Pacific convection oscillation and summer surface air temperature in Southern Asia. *Sola* **13**, 199–204 (2017).
23. Bjerknes, J. Atmospheric telecconnections from equatorial Pacific. *Mon. Weather Rev.* **97**, 163–172 (1969).
24. Wang, B., Wu, R. G. & Fu, X. H. Pacific-East Asian teleconnection: how does ENSO affect East Asian climate? *J. Clim.* **13**, 1517–1536 (2000).
25. Wu, Z. W., Wang, B., Li, J. P. & Jin, F. F. An empirical seasonal prediction model of the east Asian summer monsoon using ENSO and NAO. *J. Geophys. Res. Atmos.* **114**, 1–13 (2009).
26. Wu, Z., Li, J., Jiang, Z., He, J. & Zhu, X. Possible effects of the North Atlantic Oscillation on the strengthening relationship between the East Asian Summer monsoon and ENSO. *Int. J. Climatol.* **32**, 794–800 (2012).
27. Kim, J.-W., Yeh, S.-W. & Chang, E.-C. Combined effect of El Niño-Southern Oscillation and Pacific Decadal Oscillation on the East Asian winter monsoon. *Clim. Dyn.* **42**, 957–971 (2014).
28. Saji, N. H., Goswami, B. N., Vinayachandran, P. N. & Yamagata, T. A dipole mode in the tropical Indian Ocean. *Nature* **401**, 360–363 (1999).
29. Xie, S. P. et al. Indo-western Pacific ocean capacitor and coherent climate anomalies in post-ENSO summer: a review. *Adv. Atmos. Sci.* **33**, 411–432 (2016).
30. Zhao, Y., Duan, A. & Wu, G. Interannual variability of late-spring circulation and diabatic heating over the Tibetan Plateau associated with Indian Ocean forcing. *Adv. Atmos. Sci.* **35**, 927–941 (2018).
31. Zuo, J., Li, W., Sun, C., Xu, L. & Ren, H.-L. Impact of the North Atlantic sea surface temperature tripole on the East Asian summer monsoon. *Adv. Atmos. Sci.* **30**, 1173–1186 (2013).
32. Jiang, L. S., Li, T. & Ham, Y. G. Critical role of tropical North Atlantic SSTA in boreal summer in affecting subsequent ENSO evolution. *Geophys. Res. Lett.* **49**, 1–10 (2022).
33. Zhu, Z. W., Lu, R., Fu, S. S. & Chen, H. Alternation of the atmospheric teleconnections associated with the Northeast China Spring Rainfall during a Recent 60-Year Period. *Adv. Atmos. Sci.* **40**, 168–176 (2023).
34. Ehsan, M. A. et al. Atlantic Ocean influence on Middle East summer surface air temperature. *npj Clim. Atmos. Sci.* **3**, 1–8 (2020).
35. Huang, B. H., Schopf, P. S. & Shukla, J. Intrinsic ocean-atmosphere variability of the tropical Atlantic Ocean. *J. Clim.* **17**, 2058–2077 (2004).
36. Handoh, I. C., Matthews, A. J., Bigg, G. R. & Stevens, D. P. Interannual variability of the tropical Atlantic independent of and associated with ENSO: Part I. The North Tropical Atlantic. *Int. J. Climatol.* **26**, 1937–1956 (2006).
37. Handoh, I. C., Bigg, G. R., Matthews, A. J. & Stevens, D. P. Interannual variability of the tropical Atlantic independent of and associated with ENSO: Part II. The South Tropical Atlantic. *Int. J. Climatol.* **26**, 1957–1976 (2006).
38. Chang, P., Fang, Y., Saravanan, R., Ji, L. & Seidel, H. The cause of the fragile relationship between the Pacific El Niño and the Atlantic Niño. *Nature* **443**, 324–328 (2006).
39. Kucharski, F., Bracco, A., Yoo, J. H. & Molteni, F. Atlantic forced component of the Indian monsoon interannual variability. *Geophys. Res. Lett.* **35**, 1–5 (2008).
40. Zhang, S. Y., Liu, Y. M., Sheng, C. & Ma, T. T. Influence of boreal spring sea surface temperature anomalies over the tropical South Atlantic on the Meiyu onset. *Clim. Dyn.* **60**, 3616–3628 (2023).
41. Sheng, C., Wu, G. X., He, B., Liu, Y. M. & Ma, T. T. Linkage between cross-equatorial potential vorticity flux and surface air temperature over the mid-high latitudes of Eurasia during boreal spring. *Clim. Dyn.* **59**, 3247–3263 (2022).
42. Yang, Y., Zhu, Z. W., Shen, X. Y., Jiang, L. S. & Li, T. M. The Influences of Atlantic Sea Surface Temperature Anomalies on the ENSO-Independent Interannual Variability of East Asian Summer Monsoon Rainfall. *J. Clim.* **36**, 677–692 (2023).
43. North, G. R., Bell, T. L., Cahalan, R. F. & Moeng, F. J. Sampling errors in the estimation of empirical orthogonal functions. *Mon. Weather Rev.* **110**, 699–706 (1982).
44. Xie, S. P. et al. Indian ocean capacitor effect on Indo-Western pacific climate during the summer following El Nino. *J. Clim.* **22**, 730–747 (2009).
45. Kucharski, F. et al. A Gill-Matsuno-type mechanism explains the tropical Atlantic influence on African and Indian monsoon rainfall. *Quart. J. Roy. Meteor. Soc.* **135**, 569–579 (2009).
46. Kosaka, Y. & Nakamura, H. Structure and dynamics of the summertime Pacific-Japan teleconnection pattern. *Quart. J. Roy. Meteor. Soc.* **132**, 2009–2030 (2006).
47. Simmons, A. J., Wallace, J. M. & Branstator, G. W. Barotropic wave-propagation and instability, and atmospheric teleconnection patterns. *J. Atmos. Sci.* **40**, 1363–1392 (1983).
48. Hoskins, B. J., James, I. N. & White, G. H. The shape, propagation and mean-flow interaction of large-scale weather system. *J. Atmos. Sci.* **40**, 1595–1612 (1983).
49. Hoskins, B., McIntyre, M. E. & Robertson, A. W. On the use and significance of isentropic potential vorticity maps. *Quart. J. Roy. Meteor. Soc.* **111**, 877–946 (1985).
50. Hoskins, B., Pedder, M. & Jones, D. W. The omega equation and potential vorticity. *Quart. J. Roy. Meteor. Soc.* **129**, 3277–3303 (2003).
51. Efron, B. Computers and the theory of statistics—thinking the unthinkable. *Siam Rev.* **21**, 460–480 (1979).
52. Diaconis, P. & Efron, B. Computer-intensive methods in statistics. *Sci. Am.* **248**, 116 (1983). -&.
53. Jin, E. K. et al. Current status of ENSO prediction skill in coupled ocean-atmosphere models. *Clim. Dyn.* **31**, 647–664 (2008).
54. Torrence, C. & Webster, P. J. The annual cycle of persistence in the El Nino Southern Oscillation. *Q. J. Roy. Meteor. Soc.* **124**, 1985–2004 (1998).
55. Webster, P. J. & Yang, S. Monsoon and Enso—selectively interactive systems. *Quart. J. Roy. Meteor. Soc.* **118**, 877–926 (1992).
56. Hersbach, H. et al. The ERA5 global reanalysis. *Q. J. Roy. Meteor. Soc.* **146**, 1999–2049 (2020).
57. Ishii, M., Shouji, A., Sugimoto, S. & Matsumoto, T. Objective analyses of sea-surface temperature and marine meteorological variables for the 20th century using icoads and the Kobe collection. *Int. J. Climatol.* **25**, 865–879 (2005).
58. Takaya, K. & Nakamura, H. A formulation of a phase-independent wave-activity flux for stationary and migratory quasigeostrophic eddies on a zonally varying basic flow. *J. Atmos. Sci.* **58**, 608–627 (2001).
59. Sheng, C. et al. Characteristics of the potential vorticity and its budget in the surface layer over the Tibetan plateau. *Int. J. Climatol.* **41**, 439–455 (2021).
60. Bao, Q. et al. Outlook for El Niño and the Indian Ocean Dipole in autumn-winter 2018-2019. *Chin. Sci. Bull.* **64**, 73–78 (2019).
61. Lin, S. J. A. "vertically Lagrangian" finite-volume dynamical core for global models. *Mon. Weather Rev.* **132**, 2293–2307 (2004).
62. He, B. et al. CAS FGOALS-f3-L Model Datasets for CMIP6 Historical Atmospheric Model Intercomparison Project Simulation. *Adv. Atmos. Sci.* **36**, 771–778 (2019).
63. He, B. et al. CAS FGOALS-f3-L Model Datasets for CMIP6 GMMIP Tier-1 and Tier-3 Experiments. *Adv. Atmos. Sci.* **37**, 18–28 (2020).

ACKNOWLEDGEMENTS

This study was funded by the National Natural Science Foundation of China (42288101), Project funded by China Postdoctoral Science Foundation

(2023M733454), and the Chinese Academy of Science Special Research Assistant project (2022000242).

AUTHOR CONTRIBUTIONS

C.S. and Y.L. conceived the study. C.S. wrote the paper. Material preparation, data collection, and drawing of schematics were accomplished with the assistance of Shaoyu Zhang. Guoxiong Wu and Bian He assisted in the interpretation of the results. All authors commented on and revised the paper.

COMPETING INTERESTS

The authors declare no competing interests.

ADDITIONAL INFORMATION

Supplementary information The online version contains supplementary material available at https://doi.org/10.1038/s41612-023-00515-y.

Correspondence and requests for materials should be addressed to Yimin Liu.